Showcasing research from Professor Kumar Varoon Agrawal's laboratory, Institute of Chemical Sciences & Engineering (ISIC), École Polytechnique Fédérale de Lausanne (EPFL), Switzerland

High-permeance polymer-functionalized single-layer graphene membranes that surpass the postcombustion carbon capture target

In this work, high-performance membrane based postcombustion carbon capture is demonstrated. These membranes have the potential to increase the energy-efficiency of carbon capture reducing the capture penalty. The authors report a new class of membrane, based on polymer-functionalized nanoporous single-layer graphene, exceeding the postcombustion capture target by a significant margin. Briefly, nanometer-thick CO_2-selective polymer layers yield a large CO_2 permeance with an attractive CO_2/N_2 selectivity. The chemistry is highly tunable with respect to the polymer and could pave the way for high-performance membranes for several critical separations.

As featured in:

See Kumar Varoon Agrawal *et al.*, *Energy Environ. Sci.*, 2019, **12**, 3305.

ROYAL SOCIETY OF CHEMISTRY | Celebrating IYPT 2019

rsc.li/ees

Registered charity number: 207890

Energy & Environmental Science

COMMUNICATION

View Article Online
View Journal | View Issue

Cite this: *Energy Environ. Sci.*, 2019, **12**, 3305

Received 18th April 2019,
Accepted 15th July 2019

DOI: 10.1039/c9ee01238a

rsc.li/ees

High-permeance polymer-functionalized single-layer graphene membranes that surpass the postcombustion carbon capture target†

Guangwei He,[a] Shiqi Huang,[a] Luis Francisco Villalobos,[a] Jing Zhao,[a] Mounir Mensi,[b] Emad Oveisi,[c] Mojtaba Rezaei[a] and Kumar Varoon Agrawal *[a]

Membrane-based postcombustion carbon capture can reduce the capture penalty in comparison to absorbent-based separation. To realize this, high-performance membranes are urgently needed with a CO_2 permeance exceeding 1000 gas permeation units or GPU, and a CO_2/N_2 mixture separation factor exceeding 20. Here, we report a new class of organic–inorganic hybrid membranes based on single-layer graphene with a selective layer thinner than 20 nm. For this, the impermeable graphene lattice is exposed to oxygen plasma leading to a high percentage of vacancy defects (porosity up to 18.5%) and is then functionalized with CO_2-philic polymeric chains. Treating a gas stream mimicking flue gas, the hybrid membranes yield a six-fold higher CO_2 permeance (6180 GPU with a CO_2/N_2 separation factor of 22.5) than the performance target. Membranes prepared with a combination of optimized graphene porosity, pore size, and functional groups yield a CO_2 permeance up to 11 790 GPU. Other membranes yield a CO_2/N_2 selectivity up to 57.2.

Broader context

Curbing anthropogenic CO_2 emissions to control global warming is currently one of the biggest technological challenges. One of the potential routes to reduce emissions is postcombustion CO_2 capture followed by sequestration or utilization. In this context, capture using high-performance CO_2-selective membranes has been identified as one of the most energy-efficient routes for reducing CO_2 emissions. High-performance membranes are environmentally-friendly (no chemical is used, no waste is generated), can intensify chemical processes, and can be employed for capture in a decentralized fashion. In this work, the authors report a new class of high-performance membranes, based on polymer functionalized single-layer graphene, which not only meets the postcombustion capture target but exceeds it by a significant margin. The reported membranes are highly tunable with respect to the functional organic layer and could pave the way for next-generation high-performance membranes for several critical separations.

The sixth assessment report by the Intergovernmental Panel on Climate Change highlights the necessity to restrict the global temperature rise to within 1.5 °C from pre-industrial levels, which requires the reduction of CO_2 emissions by 45% in 2030, compared to that in 2010.[1] An energy-efficient implementation of carbon capture is extremely critical for this.[2] The captured CO_2 can be either sequestered or converted into useful chemicals, leading to a negligible overall carbon footprint. Commercial, absorption-based CO_2 capture leads to a high energy penalty attributed to its dependence on thermal energy for absorbent regeneration.[3–5] Moreover, scrubbing technology suffers from the oxidative degradation of amines and is not environmentally friendly due to the loss of amines during the regeneration step.[6] In comparison, high-performance membranes can cut down the capture cost from CO_2-rich flue-gas streams, especially those from the steel and cement industries with CO_2 concentrations reaching 20%, mainly because they do not rely on relatively expensive thermal energy but instead on mechanical energy to create a concentration gradient across the membrane.[5,7–11] For example, a two-stage membrane process, using flue gas compressed to 2 bar and using an aspirator on the permeate side, has been shown to capture 90% of CO_2 while restricting the capture cost to below $40 per ton of captured CO_2.[5] A number of studies have shown that the membrane-process becomes competitive with commercial absorption processes when the CO_2 permeance (transmembrane pressure-normalized flux) exceeds 1000 gas permeation units (GPU; 1 GPU = 3.35×10^{-10} mol m^{-2} s^{-1} Pa^{-1}) and the CO_2/N_2 separation factor exceeds 20.[5,12–16] The capital cost of the membrane modules is inversely proportional to the CO_2 permeance. Increasing the membrane permeance beyond the target of 1000 GPU is therefore seen as the way forward for boosting the case of membrane-based

[a] *Laboratory of Advanced Separations (LAS), École Polytechnique Fédérale de Lausanne (EPFL), Sion, Switzerland. E-mail: kumar.agrawal@epfl.ch*
[b] *Institute of Chemical Sciences and Engineering (ISIC), EPFL, Sion, Switzerland*
[c] *Innovation Interdisciplinary Centre for Electron Microscopy (CIME), EPFL, Lausanne, Switzerland*

† Electronic supplementary information (ESI) available: Experimental methods and supporting figures. See DOI: 10.1039/c9ee01238a

carbon capture.[17–23] However, currently, the preparation of membranes that reach a CO_2 permeance significantly higher than 1000 GPU while meeting the separation factor target of 20 remains an important challenge.

Dense membranes based on conventional polymeric materials suffer from an intrinsic permeability–selectivity tradeoff.[24] So far, the second-generation Polaris™ membranes have yielded the best performance among polymeric membranes with the permeance reaching 2000 GPU with a CO_2/N_2 separation factor of 50.[25] Facilitated-transport membranes offer attractive permeance and selectivity, however, their application is hindered by the stability issues as well as the need for water scavenging from the permeate stream (Supplementary note I, ESI†).[26–31] Stacked graphene oxide (GO) nanosheet based membranes have demonstrated high CO_2/N_2 selectivities, however, the CO_2 permeance has remained limited to *ca.* 500 GPU, attributed to the tortuous, several micrometers long diffusion path of CO_2.[32,33] Cell membrane proteins serving as ion channels for the rapid yet selective transport of ions represent an ideal membrane where the rapid separation results from a narrow passage in the protein structure.[28] Likewise, nanoporous two-dimensional films hosting a moderate to high-density of molecular-selective pores can yield a high gas permeance with an attractive separation selectivity.[34] Recently, we demonstrated the separation of gas molecules from single-layer graphene by the size-sieving mechanism, with a sieving-resolution of 1 Å (for example, H_2 from CH_4).[35] For postcombustion capture, one needs to separate CO_2 from N_2, where the difference in the kinetic diameters is only 0.3 Å. A way forward to achieve this is to functionalize the graphene surface with CO_2-philic groups, which can enhance the selective adsorption of CO_2 from the gas phase to the graphene nanopores.[36]

Here, we demonstrate this concept for the first time, leading to CO_2-selective nanoporous graphene membranes yielding a CO_2 permeance (6180 GPU) that is six-fold higher than that of the capture target, and a corresponding CO_2/N_2 mixture separation factor of 22.5. We developed a series of millimeter-sized swollen, polymer-functionalized nanoporous graphene (SPONG) membranes with selective layers that are only up to 20 nm thick, and yield record-high postcombustion capture performance from a gas mixture mimicking the flue gas streams. Other membranes, prepared with a combination of graphene porosity (percentage of the area covered by vacancy defects), pore size (diameter of the vacancy defects), and functional groups, yielded a combination of attractive CO_2 permeance and CO_2/N_2 selectivity with permeance up to 11 790 GPU and selectivity up to 57.2.

SPONG membranes and their carbon capture performance

The fabrication of SPONG membranes is illustrated in Fig. 1. First, oxygen-functionalized nanoporous graphene (ONG) was obtained by exposing single-layer graphene to oxygen plasma and ozone. Subsequently, CO_2-philic polymeric chains were grafted on the porous graphene lattice to obtain polymer-functionalized ONG (PONG). Last, the poly(ethylene glycol)-dimethyl-ether (PEGDE) oligomer was used to swell the CO_2-philic polymer layer in PONG leading to a swollen PONG (SPONG) film with a total film thickness of less than 20 nm. The atom-thick nanoporous graphene matrix (ONG) and the CO_2-selective polymeric layer act synergistically to allow fast and selective transport of CO_2 (Supplementary note II, ESI†). The SPONG layer was mechanically reinforced by a thin film of poly-[1-(trimethylsilyl)-1-propyne] or PTMSP to prevent cracks and tears in the SPONG layer.

Several SPONG membranes were prepared where the mean pore size and the porosity of graphene were varied between 1.8 to 3.3 nm, and 6.8 to 18.5%, respectively. Two CO_2-philic polymers, polyethylenimine (PEI) and poly(ethylene glycol)-bis-amine (PEGBA), were evaluated. The separation performance was characterized using a homemade gas permeance setup, with the feed pressurized to 2 bar, and the permeate maintained at 1 bar. The transport properties of single component CO_2 and N_2 as well as a 20/80 (v/v) CO_2/N_2 mixture, representing the typical emissions from the steel and the cement industries, were probed. Overall, several membranes displayed selective CO_2 transport with a CO_2/N_2 separation factor greater than 20 and with a CO_2 permeance significantly higher than 1000 GPU (Table 1).

The separation performance showed a strong dependence on the pore size in graphene, the choice of CO_2-philic polymer, and the permeation temperature (Fig. 2). An increase in the mean pore size in graphene led to an increase in the CO_2 permeance, albeit with a decrease in the CO_2/N_2 selectivity (Fig. 2a and b). The permeance trend can be attributed to the fact that the graphene porosity increased with increasing the pore size (refer to the characterization of graphene in a later section).

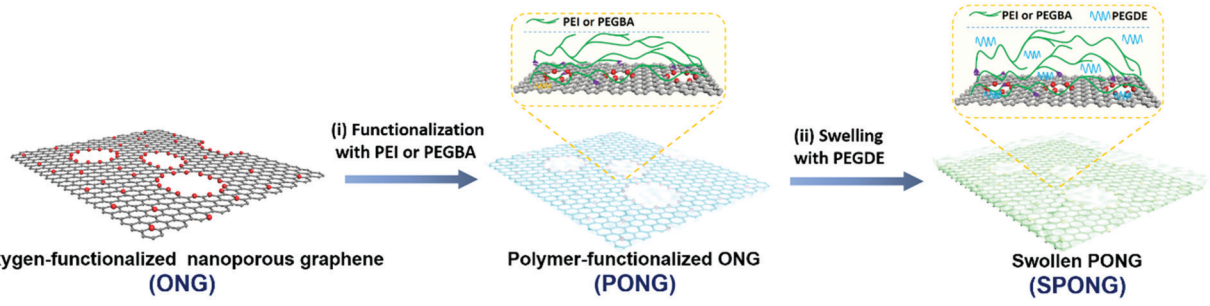

Fig. 1 Schematic illustration of the preparation and the structure of the SPONG membrane.

Table 1 CO_2 permeance, and CO_2/N_2 and CO_2/CH_4 ideal selectivity of SPONG membranes under single-gas permeation conditions at 30 °C, 2 bar

CO_2-philic polymer	Mean pore size (nm)	Membrane nomenclature	CO_2 permeance (GPU)	CO_2/N_2 ideal selectivity	CO_2/CH_4 ideal selectivity
PEI	1.8	M1-PEI-4s	1040	41.9	18.6
PEI	1.8	M2-PEI-4s	1070	36.6	15.8
PEI	1.8	M3-PEI-4s	1000	42.3	17.9
PEI	2.4	M4-PEI-6s	5540	25.2	10.9
PEI	2.4	M5-PEI-6s	6290	20.4	9.3
PEI	2.4	M6-PEI-6s	4420	24.8	10.0
PEI	2.4	M7-PEI-6s	3730	28.9	10.9
PEI	3.3	M8-PEI-8s	11 790	14.7	7.5
PEI	3.3	M9-PEI-8s	9340	16.7	8.0
PEI	3.3	M10-PEI-8s	10 320	17.7	8.9
PEGBA	1.8	M11-PEGBA-4s	630	57.2	20.5
PEGBA	2.4	M12-PEGBA-6s	1250	35.1	14.4
PEGBA	3.3	M13-PEGBA-8s	4420	20.8	9.3

We did not detect CO_2 permeation when the graphene lattice was not etched (Fig. 2b). On the other hand, it becomes increasingly difficult to effectively mask graphene pores larger than 2 nm by the few-nanometer-thick CO_2-philic layer (Supplementary note II, ESI†). As a result, a tradeoff between the CO_2 permeance and the CO_2/N_2 selectivity was observed as a function of the mean pore size. In future, this tradeoff can be reduced or eliminated by developing methods that generate high porosity in graphene while restricting the pore size to below 2 nm.

When the polymer functionalization was not carried out on ONG, the CO_2/N_2 selectivity was limited to 12, close to the selectivity expected from the mechanically reinforcing PTMSP layer (control data, Fig. 2c). Again, in this case, we could not detect CO_2 transport when the graphene lattice was not etched. The functionalization of ONG with PEI or PEGBA followed by subsequent swelling with PEGDE led to a significantly increase in the CO_2/N_2 selectivity, attributed to the fact that the CO_2-philic chains can effectively promote the preferential adsorption of CO_2 (Supplementary note II, ESI†).

The CO_2 permeance and the CO_2/N_2 selectivity from the non-swollen membranes (PONG) were lower than those from the corresponding swollen (SPONG) membranes (Table S1, ESI†). The impregnation of PEGDE into the PEI (or PEGBA) network is expected to alter the hydrogen-bonding network of PEI (or PEGBA).[37,38] The analysis of the free volume or chain packing in few-nanometer-thick polymer films confined around nanoporous graphene lattices is challenging, and we hope to characterize the exact nature of these structural changes in the future. Based on the performance trend (improvement in the CO_2 permeance as well as the CO_2/N_2 selectivity) from the gas permeation data, it is clear that compared to the amine groups of PEI, the ethylene oxide groups of PEGDE were more effective in the selective transport of CO_2. This was also evident from the fact the PEGBA-based PONG and SPONG membranes, hosting predominantly ethylene oxide groups, yielded higher selectivities than those from the PEI-based PONG and SPONG membranes (Table 1 and Table S1, ESI†).

The mixed gas separation performance of the SPONG membranes was similar to that from the single-component gas permeation (Fig. 2a and Table S2, ESI†), making these membranes highly attractive for carbon capture application.

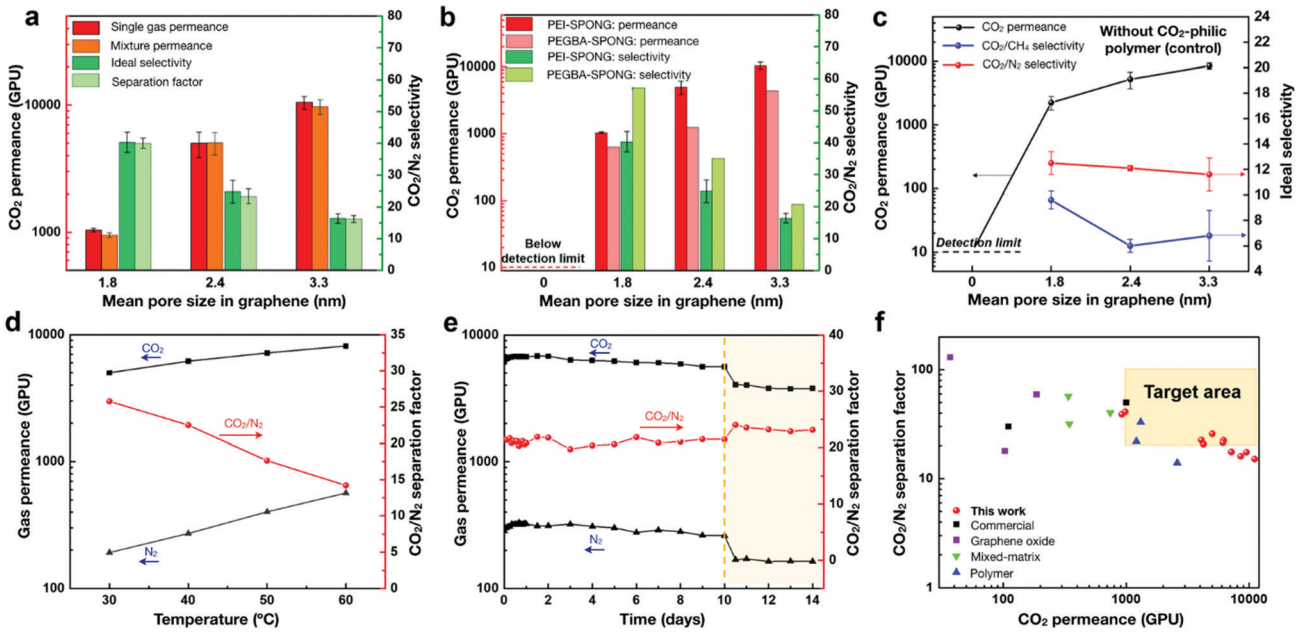

Fig. 2 Carbon capture performance of the SPONG membranes. CO_2 permeance and CO_2/N_2 selectivity as a function of the mean pore size in graphene for (a) PEI-based SPONG (single gas and mixture data), and (b) PEI- and PEGBA-based SPONG (single gas data). (c) Control data from graphene without using the CO_2-philic polymer. The gas permeance and CO_2/N_2 separation factor as a function of (d) temperature (M4, PEI-based SPONG), and (e) time in days (M5, PEI-based SPONG). Saturated water vapor was introduced to the feed side after 10 days of testing. (f) CO_2/N_2 mixture separation performance of SPONG membranes compared with that from the state-of-the-art membranes (Table S4, ESI†). The target performance zone is highlighted in peach. All membranes have a thin PTMSP layer as a mechanical reinforcement.

The CO_2 and N_2 permeances were temperature-activated, and the permeances increased as a function of temperature (Fig. 2d). The apparent activation energy, defined as the sum of the heat of sorption and the activation energy of diffusion, was positive. Since the heat of sorption is negative and the activation energy of diffusion is positive, this indicates that the activation energy for diffusion was higher than the heat of sorption. This is typically observed when the molecules interact strongly with a narrow transport path in the media where the transport of the molecules is resisted by the media. The apparent activation energy of N_2 (31 kJ mol^{-1}) was significantly higher than that of CO_2 (14 kJ mol^{-1}), attributed to the larger size of N_2 (a kinetic diameter of 3.6 Å for N_2 in comparison to that of 3.3 Å for CO_2). Therefore, while both the CO_2 and N_2 permeances increased with temperature, the N_2 permeance increased more rapidly, thus resulting in the reduction of the CO_2/N_2 separation factor with the temperature rise (Fig. 2d). This can be exploited at the process engineering stage, where the operating temperature can be used to optimize the permeance and selectivity to obtain the desired recovery and purity.

The SPONG membranes displayed resistance to physical aging. The CO_2 permeance increased from 6110 to 6800 GPU during the initial 2 days and then decreased to 5610 GPU during the subsequent 8 days, while the separation factor did not change, and remained close to 20 (Fig. 2e). Subsequently, the feed stream was saturated with water, which increased the selectivity to 24. This can be attributed to the activation of ternary amine sites of PEI for CO_2 sorption. A sharp permeance decrease to 4050 GPU was observed, which stabilized to 3780 GPU in the next 2 days. We hypothesize that the decrease in permeance could be due to increased resistance in the polymer layer attributed to the water-led acceleration of the physical aging of the polymer chains. Despite this, the stabilized CO_2 permeance, 3780 GPU, is more than three-fold higher than the performance target for carbon capture (1000 GPU), making SPONG membranes extremely attractive for CO_2 capture from flue gas saturated with water vapor.[33] Also, as a result of the selective CO_2 permeance, attractive CO_2/CH_4 selectivities, up to 20, were also achieved (Table 1 and Fig. S1, ESI†), making these membranes applicable to natural gas sweetening and biogas upgrading.

The permeability (the permeance multiplied by the thickness of the selective layer) of the membranes offering the best combination of CO_2 permeance and CO_2/N_2 selectivity was estimated by a resistance model (Table S3, ESI†).[39] M5-PEI-6s yielded a CO_2 permeability of 213 Barrer with a CO_2/N_2 selectivity of 27.5. While this is not the highest permeability when compared to other CO_2-selective membranes (Table S4, ESI†), we would like to point out that permeance rather than permeability is the direct indicator of membrane-based carbon capture performance. For example, the outstanding separation performance of the SPONG membranes is established by comparing the gas mixture separation data with those from the state-of-the-art membranes (Fig. 2f, Table S4 and Supplementary note I, ESI†). The target performance zone indicates that the membrane should yield a CO_2 permeance higher than 1000 GPU and a separation factor higher than 20 to achieve economical capture compared to the amine-based absorption process.[5] The M4-PEI-6s membrane showed an exceptionally high CO_2 permeance of 5010 GPU with a moderate CO_2/N_2 separation factor of 25.8 at 30 °C. At 40 °C, the CO_2 permeance increased to 6180 GPU while the CO_2/N_2 separation factor, 22.5, remained in the target area. It has been shown that beyond a selectivity of 30, the capture cost does not change significantly with increasing selectivity.[5] Since the needed membrane area is inversely proportional to the permeance, enhancing the CO_2 permeance at a fixed selectivity can decrease the cost of installation of the membrane unit (capital cost) and increase the competitiveness of the membrane process for carbon capture.

The microstructure of SPONG membranes

To elucidate the microstructure of the SPONG membranes, we employed Raman spectroscopy, electron microscopy, X-ray photoelectron spectroscopy (XPS), and atomic force microscopy (AFM). Raman spectroscopy confirmed that the as-synthesized graphene was single-layer with an I_{2D}/I_G ratio of 3.26 ± 0.32, where I_G and I_{2D} represent the peak heights of the G and 2D peaks, respectively (Fig. 3a and Fig. S2, ESI†). Since the pristine graphene lattice is impermeable to molecules, we employed the scalable O_2 plasma-based etching[40–42] to generate a high-density of nanometer-sized pores leading to nanoporous graphene (NG). To estimate the vacancy-defects in the NG lattice by Raman spectroscopy, NG was

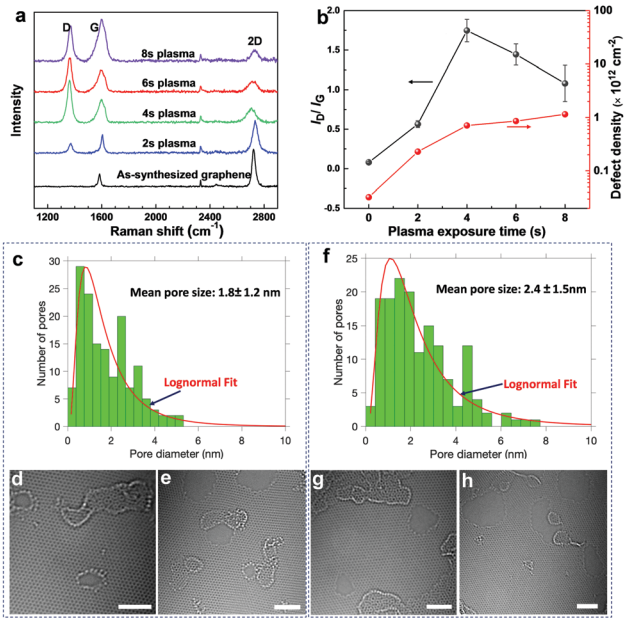

Fig. 3 Characterization of the pore structure and pore-size-distribution in graphene. (a) Raman spectra of as-synthesized graphene and graphene exposed to plasma for various times. (b) Plots of I_D/I_G and the defect-density as a function of the plasma exposure time. (c–h) Aberration-corrected TEM images and the corresponding pore-size-distribution of NG prepared by plasma treatment for 4 s (c–e) and 6 s (f–h). The mean pore size corresponds to the arithmetic average of the pore diameters. The scale bars in the images correspond to 2 nm.

heated to 300 °C in a reducing atmosphere. Heat treatment in a reducing atmosphere is known to eliminate the sp^3-defects as well as the physisorbed species on graphene.[43,44] Subsequent Raman analysis revealed that the defect-density, characterized by the I_D/I_G ratio, increased with increasing the plasma time (Fig. 3a and b). The D peak in the Raman spectrum, originating from the breathing of the six-atom ring in the graphene lattice, is activated by the presence of defects and therefore the I_D/I_G ratio can be used to calculate the defect-density in graphene (Fig. 3b, Supplementary note III, ESI†).[45] The defect-density monotonically increased with the plasma exposure time, from 0.7×10^{12} to 1.2×10^{12} cm^{-2} between 4 and 8 s (Fig. 3b). While the intensity of the 2D peak reduced with the plasma time (Fig. S2, ESI†), the presence of a significant 2D peak even at 8 s of plasma treatment indicates that graphene was not amorphized during the plasma treatment.

Aberration-corrected high-resolution transmission electron microscopy (HRTEM) revealed that NG was indeed comprised of a high-density of nanopores, consistent with the Raman analysis. Typically, the presence of polymer contamination/residues on the graphene lattice can lead to pore-nucleation and/or expansion under the electron beam. Therefore, for an accurate estimation of the pore-size-distribution, we developed a contamination-free transfer technique. A novel carbon-film-assisted transfer method was used to transfer graphene to the TEM grid while completely avoiding any polymeric contamination (Supplementary note IV, Fig. S3, ESI†). As a result, extremely stable imaging conditions were obtained where neither pore-nucleation nor expansion was observed during imaging (Supplementary Video, ESI†). Based on HRTEM observations, the nanopores had a log-normal distribution, with a mean pore size (arithmetic average of the pore diameters) of 1.8 ± 1.2 and 2.4 ± 1.5 nm after 4 and 6 s of plasma treatment, respectively (Fig. 3c–h). Several large nanopores (up to 5 and 8 nm in the 4 and 6 s samples, respectively) were also present. Both zigzag and armchair pore-edge configurations could be observed. Overall, at 4 and 6 s, the pore-densities were 2.1×10^{12} and 2.3×10^{12} cm^{-2}, respectively, corresponding to porosities of 6.8 and 13%, respectively (Fig. S4a and b, ESI†). The order of magnitude of the pore-density obtained by electron microscopy is consistent with the defect-density from the Raman analysis (Table S5, ESI†). While new pores were nucleated as the etching time was increased, the mean pore size increased at a linear rate (4 Å s^{-1}) with respect to the etching time (Fig. S4a and c, ESI†). Based on this, the mean pore size in NG etched for 8 s is estimated to be around 3.2 nm.

For the eventual functionalization of the nanoporous graphene lattice with PEI or PEGBA, epoxy groups were introduced on the NG lattice by room-temperature ozone-treatment.[46] XPS confirmed successful oxidation of NG by ozone, forming ONG, with a concentration of epoxy (~285.5 eV) and carbonyl groups (~288 eV) of 7.4% and 4.0%, respectively, corresponding to a C/O ratio of 7.8 (Fig. 4a). Apart from the direct covalent functionalization with the polymer, the presence of oxygen-based functional groups in ONG is expected to improve the interaction with the amine and ethylene-oxide groups of the polymer *via* hydrogen-bonding and electrostatic interactions.[47,48] The functionalization with the polymer was made possible by the ring-opening chemistry between the epoxy group and the amine group in the polymer chains.[47] To probe the nature of the bonding between ONG and PEI, ONG was coated with a dilute aqueous solution of PEI (1 wt%), following which the film was rinsed with water to remove the excess PEI. The XPS spectra from the resulting film revealed significantly higher C1s peaks at 284.8 and 285.5 eV, essentially from the sp^3-hybridized C–C and C–N groups of PEI, indicating successful incorporation of the polymer on ONG (Fig. 4b and Tables S6, S7, ESI†). The N1s binding energy from PEI shifted from 399.0 to 399.6 eV, indicating a changing electrostatic environment around the N atoms, evidence of chemical bonding between PEI and ONG (Fig. 4c and Table S8, ESI†).[49,50] The functionalization of ONG with PEGBA was also confirmed by XPS, showing a similar result to that of PEI-based PONG (Fig. S5 and Tables S6–S8, ESI†).

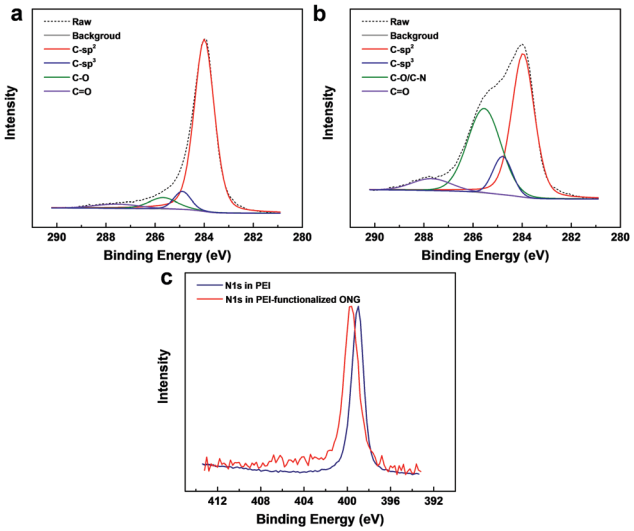

Fig. 4 XPS spectra of ONG (a) and PEI-functionalized ONG (b). (c) Comparison of the binding energy of N1s peaks from PEI-functionalized ONG with a PEI reference sample.

To ensure complete elimination of the effusive transport of gas molecules across the graphene nanopores, the polymer functionalization of graphene (PONG) was achieved by spin-coating a few nanometer-thick film of CO_2-philic polymers (PEI or PEGBA) on ONG. The AFM topography image of the resulting PEI-based PONG films indicated a smooth surface with a root mean square (RMS) surface roughness of 0.9 nm (Fig. 5a). The underlying Cu grain-boundaries and graphene wrinkles are clearly visible in the scanning electron microscopy (SEM) images, indicating that the PEI layer was extremely thin (Fig. 5b and Fig. S6, S7, ESI†). To confirm the thickness of PEI, we fabricated the PONG film on a Si wafer and made a scratch on the film revealing the underlying Si surface (Fig. 5c). A height distribution map of the area comprising the bare Si surface and PEI-coated graphene indicates that the thickness of the PEI-coated graphene film was only 10 nm (Fig. 5d). The microstructure of PEGBA-based PONG was similar to that of PEI-based PONG, albeit with a slightly higher RMS surface roughness (4.2 nm, Fig. S8 and S9, ESI†) and slightly lower thickness (Fig. S10, ESI†).

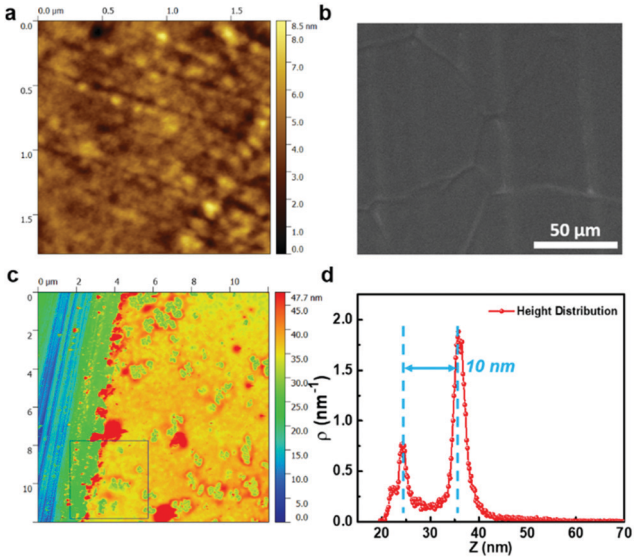

Fig. 5 Characterization of the morphology of the PEI-based PONG film. AFM topographical (a) and SEM (b) images of the as-prepared film. (c) AFM topographical image of the PONG film transferred to a Si wafer where a scratch was deliberately created to reveal the thickness of the PONG film. (d) Height distribution of the area covered by the black square in (c) revealing that the PEI-based PONG film was only 10 nm thick.

To prevent cracks and tears in the nanometer-thick PONG film during its transfer from Cu to the porous support, the PONG film was reinforced with a PTMSP layer. A 100% success rate, defined by the number of crack-free membranes normalized by the number of attempts, was achieved for over 100 samples. PTMSP is one of the most permeable polymers with an ultrahigh CO_2 permeability[51] and therefore the gas permeance from the PTMSP layer is not expected to limit the overall permeance. Sub-500 nm thick PTMSP films provided sufficient mechanical support to the floating PONG films post-copper-etching, preventing cracks and tears. Recently, we reported a nanoporous carbon film based reinforcement for crack-free transfer of graphene.[35] However, this approach requires a high-temperature pyrolysis step, which is not compatible with functional organic layers on graphene. Therefore, the PTMSP approach introduced here is uniquely appropriate as a mechanical support for organo-functionalized graphene membranes, such as the one in this work.

The last step in the preparation of the SPONG membranes was swelling of the PONG films with PEGDE. This was carried out by simply floating the PONG film in a bath consisting of a dilute solution of PEGDE oligomer (2 mg mL^{-1}). The hydrodynamic diameter of a PEG oligomer with a MW of 500 g mol^{-1} is *ca.* 1.0 nm,[52] smaller than the size of the graphene nanopores studied here, allowing the PEGDE chains to diffuse to the exposed PEI (or PEGBA) domains across the porous graphene barrier. Interestingly, the thickness increase due to swelling with PEGDE was less than 10 nm (Fig. S11 and S12, Supplementary note V, ESI†), making the selective layer in the SPONG membranes one of the thinnest selective layers ever reported.

Conclusions

In summary, we report a new class of organic–inorganic hybrid membranes, based on nanoporous single-layer graphene functionalized with CO_2-philic polymeric chains. The synergistic properties of the nanoporous graphene matrix and CO_2-philic polymers enabled the fabrication of one of the thinnest CO_2-selective membranes. As a result, the membranes not only met the performance target for CO_2 capture but also yielded a record CO_2 permeance. For example, a CO_2 permeance of 6180 GPU with a CO_2/N_2 separation factor of 22.5 was achieved.

This approach allows one to apply low-molecular-weight polymers and oligomers for carbon capture, which is usually difficult to implement because of mechanical stability issues. Overall, the approach of functionalizing ONG with a CO_2-philic molecule is generic, opening opportunities for further optimization of the separation performance by using tailor-made functional groups. The recent development in the scale-up of single-layer graphene membranes can be adopted to scaling SPONG based membranes (Supplementary note VI, ESI†).[53] Considering the exceptional performance and the high tunability potential of this hybrid approach, it could pave the way for next-generation high-performance membranes for several critical separations.

Author contributions

KVA and GH conceived the project. GH designed, prepared and characterized the graphene-based membranes. SH and JZ developed the porous graphene. LFV, SH and JZ developed the method of preparing HRTEM samples. JZ carried out the Raman spectroscopy. MM performed the AFM and XPS experiments. EO characterized graphene with HRTEM. MR performed the EDS experiments. KVA and GH wrote the manuscript. All authors revised the paper.

Conflicts of interest

KVA and GH have filled a patent application based on these findings.

Acknowledgements

The authors acknowledge our host institution, EPFL, for generous support. This work was also supported by the ETH board, GAZNAT, Swiss National Science Foundation (Assistant Professor Energy Grant; grant number: PYAPP2_173645), and the Swiss Competence Center for Energy Research – Efficiency in Industrial Processes (SCCER-EIP, Phase II; grant number: 1155002538). GH acknowledges funding from the European Union's Horizon 2020 Research and innovation programme under the Marie Skłodowska-Curie grant agreement No. 665667. The authors acknowledge Prof. Giovanni Dietler and Caroline Lehman (EPFL, LPMV) for the access to the AFM laboratory, and acknowledge Dr. Wen Luo and Prof. Andreas Züttel (EPFL, LMER) for XPS characterization.

Notes and references

1 6th Intergovernmental Panel on Climate Change (IPCC) Report Online, https://www.ipcc.ch/report/sixth-assessment-report-working-group-ii/, accessed 2018.
2 R. S. Haszeldine, *Science*, 2009, **325**, 1647–1652.
3 G. T. Rochelle, *Science*, 2009, **325**, 1652–1654.
4 L.-C. Lin, A. H. Berger, R. L. Martin, J. Kim, J. A. Swisher, K. Jariwala, C. H. Rycroft, A. S. Bhown, M. W. Deem, M. Haranczyk and B. Smit, *Nat. Mater.*, 2012, **11**, 633.
5 T. C. Merkel, H. Lin, X. Wei and R. Baker, *J. Membr. Sci.*, 2010, **359**, 126–139.
6 A. B. Rao and E. S. Rubin, *Environ. Sci. Technol.*, 2002, **36**, 4467–4475.
7 B. Ghalei, K. Sakurai, Y. Kinoshita, K. Wakimoto, A. P. Isfahani, Q. Song, K. Doitomi, S. Furukawa, H. Hirao, H. Kusuda and S. Kitagawa, *Nat. Energy*, 2017, **2**, 17086.
8 T.-H. Bae, M. R. Hudson, J. A. Mason, W. L. Queen, J. J. Dutton, K. Sumida, K. J. Micklash, S. S. Kaye, C. M. Brown and J. R. Long, *Energy Environ. Sci.*, 2013, **6**, 128–138.
9 J. E. Bara, D. E. Camper, D. L. Gin and R. D. Noble, *Acc. Chem. Res.*, 2009, **43**, 152–159.
10 Z. Qiao, S. Zhao, J. Wang, S. Wang, Z. Wang and M. D. Guiver, *Angew. Chem., Int. Ed.*, 2016, **128**, 9467–9471.
11 L. Zhu, M. T. Swihart and H. Lin, *Energy Environ. Sci.*, 2018, **11**, 94–100.
12 Z. Qiao, S. Zhao, M. Sheng, J. Wang, S. Wang, Z. Wang, C. Zhong and M. D. Guiver, *Nat. Mater.*, 2018, **18**, 163.
13 K. Xie, Q. Fu, C. Xu, H. Lu, Q. Zhao, R. Curtain, D. Gu, P. A. Webley and G. G. Qiao, *Energy Environ. Sci.*, 2018, **11**, 544–550.
14 N. Du, H. B. Park, G. P. Robertson, M. M. Dal-Cin, T. Visser, L. Scoles and M. D. Guiver, *Nat. Mater.*, 2011, **10**, 372.
15 E. Favre, *J. Membr. Sci.*, 2007, **294**, 50–59.
16 S. Roussanaly, R. Anantharaman, K. Lindqvist, H. Zhai and E. Rubin, *J. Membr. Sci.*, 2016, **511**, 250–264.
17 K. Celebi, J. Buchheim, R. M. Wyss, A. Droudian, P. Gasser, I. Shorubalko, J.-I. Kye, C. Lee and H. G. Park, *Science*, 2014, **344**, 289–292.
18 T. Rodenas, I. Luz, G. Prieto, B. Seoane, H. Miro, A. Corma, F. Kapteijn, F. X. L. i. Xamena and J. Gascon, *Nat. Mater.*, 2015, **14**, 48.
19 E. Barankova, X. Tan, L. F. Villalobos, E. Litwiller and K. V. Peinemann, *Angew. Chem., Int. Ed.*, 2017, **56**, 2965–2968.
20 L. Chen, G. Shi, J. Shen, B. Peng, B. Zhang, Y. Wang, F. Bian, J. Wang, D. Li, Z. Qian, G. Xu, G. Liu, J. Zeng, L. Zhang, Y. Yang, G. Zhou, M. Wu, W. Jin, J. Li and H. Fang, *Nature*, 2017, **550**, 380.
21 G. Liu, V. Chernikova, Y. Liu, K. Zhang, Y. Belmabkhout, O. Shekhah, C. Zhang, S. Yi, M. Eddaoudi and W. J. Koros, *Nat. Mater.*, 2018, **17**, 283–289.
22 H. B. Park, C. H. Jung, Y. M. Lee, A. J. Hill, S. J. Pas, S. T. Mudie, E. Van Wagner, B. D. Freeman and D. J. Cookson, *Science*, 2007, **318**, 254–258.
23 P. R. Kidambi, G. D. Nguyen, S. Zhang, Q. Chen, J. Kong, J. Warner, A. P. Li and R. Karnik, *Adv. Mater.*, 2018, **30**, 1804977.
24 H. B. Park, J. Kamcev, L. M. Robeson, M. Elimelech and B. D. Freeman, *Science*, 2017, **356**, 1138–1148.
25 U.S. Department of Energy office of scientific and technical information Online, https://www.osti.gov/biblio/1337555, accessed September 2015.
26 R. D. Noble, *J. Membr. Sci.*, 1991, **56**, 229–234.
27 J. Huang, J. Zou and W. S. W. Ho, *Ind. Eng. Chem. Res.*, 2008, **47**, 1261–1267.
28 Y. Fu, Y.-B. Jiang, D. Dunphy, H. Xiong, E. Coker, S. Chou, H. Zhang, J. M. Vanegas, J. G. Croissant, J. L. Cecchi, S. B. Rempe and C. J. Brinker, *Nat. Commun.*, 2018, **9**, 990.
29 F. Zhou, H. N. Tien, W. L. Xu, J. T. Chen, Q. Liu, E. Hicks, M. Fathizadeh, S. Li and M. Yu, *Nat. Commun.*, 2017, **8**, 2107.
30 Y. Han, W. Salim, K. Chen, D. Wu and W. S. W. Ho, *J. Membr. Sci.*, 2019, **575**, 242–251.
31 M. Wang, Z. Wang, S. Li, C. Zhang, J. Wang and S. Wang, *Energy Environ. Sci.*, 2013, **6**, 539–551.
32 S. Wang, Y. Wu, N. Zhang, G. He, Q. Xin, X. Wu, H. Wu, X. Cao, M. D. Guiver and Z. Jiang, *Energy Environ. Sci.*, 2016, **9**, 3107–3112.
33 S. Wang, Y. Xie, G. He, Q. Xin, J. Zhang, L. Yang, Y. Li, H. Wu, Y. Zhang, M. D. Guiver and Z. Jiang, *Angew. Chem., Int. Ed.*, 2017, **56**, 14246–14251.
34 L. Wang, M. S. H. Boutilier, P. R. Kidambi, D. Jang, N. G. Hadjiconstantinou and R. Karnik, *Nat. Nanotechnol.*, 2017, **12**, 509.
35 S. Huang, M. Dakhchoune, W. Luo, E. Oveisi, G. He, M. Rezaei, J. Zhao, D. T. L. Alexander, A. Züttel, M. S. Strano and K. V. Agrawal, *Nat. Commun.*, 2018, **9**, 2632.
36 Z. Tian, S. M. Mahurin, S. Dai and D. en Jiang, *Nano Lett.*, 2017, **17**, 1802–1807.
37 X. Jiang, S. Li and L. Shao, *Energy Environ. Sci.*, 2017, **10**, 1339–1344.
38 A. Car, C. Stropnik, W. Yave and K.-V. Peinemann, *Sep. Purif. Technol.*, 2008, **62**, 110–117.
39 Q. Fu, J. Kim, P. A. Gurr, J. M. P. Scofield, S. E. Kentish and G. G. Qiao, *Energy Environ. Sci.*, 2016, **9**, 434–440.
40 S. P. Surwade, S. N. Smirnov, I. V. Vlassiouk, R. R. Unocic, G. M. Veith, S. Dai and S. M. Mahurin, *Nat. Nanotechnol.*, 2015, **10**, 459–464.
41 M. S. H. Boutilier, D. Jang, J. C. Idrobo, P. R. Kidambi, N. G. Hadjiconstantinou and R. Karnik, *ACS Nano*, 2017, **11**, 5726–5736.
42 P. R. Kidambi, D. Jang, J. C. Idrobo, M. S. H. Boutilier, L. Wang, J. Kong and R. Karnik, *Adv. Mater.*, 2017, **29**, 1–8.
43 Y. C. Cheng, T. P. Kaloni, Z. Y. Zhu and U. Schwingenschlögl, *Appl. Phys. Lett.*, 2012, **101**, 73110.
44 Y. Mulyana, M. Uenuma, Y. Ishikawa and Y. Uraoka, *J. Phys. Chem. C*, 2014, **118**, 27372–27381.
45 A. C. Ferrari and D. M. Basko, *Nat. Nanotechnol.*, 2013, **8**, 235–246.
46 G. Lee, B. Lee, J. Kim and K. Cho, *J. Phys. Chem. C*, 2009, **113**, 14225–14229.
47 M. Wang, X. Duan, Y. Xu and X. Duan, *ACS Nano*, 2016, **10**, 7231–7247.

48 J. Zou and F. Kim, *Nat. Commun.*, 2014, **5**, 5254.
49 C. Morant, J. Andrey, P. Prieto, D. Mendiola, J. M. Sanz and E. Elizalde, *Phys. Status Solidi A*, 2006, **203**, 1069–1075.
50 K. Artyushkova, B. Kiefer, B. Halevi, A. Knop-Gericke, R. Schlogl and P. Atanassov, *Chem. Commun.*, 2013, **49**, 2539–2541.
51 D. Gomes, S. P. Nunes and K.-V. Peinemann, *J. Membr. Sci.*, 2005, **246**, 13–25.
52 H. Lee, R. M. Venable, A. D. MacKerell Jr and R. W. Pastor, *Biophys. J.*, 2008, **95**, 1590–1599.
53 Y. Yang, X. Yang, L. Liang, Y. Gao, H. Cheng, X. Li, M. Zou, R. Ma, Q. Yuan and X. Duan, *Science*, 2019, **364**, 1057–1062.

